DISCLAIMER

SANDIA REPORT
SAND2025-00306
Printed January 2025

Sandia National Laboratories

Aeroelastic Validation of the Sandia Offshore Wind Energy Simulator (OWENS) for Vertical-Axis Wind Turbines

Kevin R. Moore & Brandon L. Ennis

Prepared by
Sandia National Laboratories
Albuquerque, New Mexico 87185
Livermore, California 94550

Issued by Sandia National Laboratories, operated for the United States Department of Energy by National Technology & Engineering Solutions of Sandia, LLC.

Available to DOE and DOE contractors from

U.S. Department of Energy
Office of Scientific and Technical Information
P.O. Box 62
Oak Ridge, TN 37831

Telephone: (865) 576-8401
Facsimile: (865) 576-5728
E-Mail: reports@osti.gov
Online ordering: http://www.osti.gov/scitech

Available to the public from

U.S. Department of Commerce
National Technical Information Service
5301 Shawnee Road
Alexandria, VA 22312

Telephone: (800) 553-6847
Facsimile: (703) 605-6900
E-Mail: orders@ntis.gov
Online order: https://classic.ntis.gov/help/order-methods

ABSTRACT

Vertical-axis wind turbines (VAWTs) offer some unique advantages over traditional designs, particularly for floating offshore and certain distributed wind applications. However, the aero-elastic modeling capabilities that exist for VAWT designs greatly lags those for the traditional horizontal-axis wind turbines (HAWTs). Differences between vertical and horizontal turbines necessitates several key additions in coupled modeling, including the aerodynamic model, as well as solving a fundamentally different structural mesh. The Offshore Wind ENergy Simulator (OWENS) is specifically formulated to fulfill these requirements. This paper presents validation cases of this tool for modal, centrifugal, gravitational, normal operation, and shutdown analyses. The aeroelastic validation is performed with increasing complexity from analytical test cases to an instrumented 500kW VAWT. Validation data are taken from the Sandia National Laboratories 34 meter research turbine. The results of the validation cases are presented and examined.

This page intentionally left blank.

CONTENTS

This page intentionally left blank.

LIST OF FIGURES

This page intentionally left blank.

LIST OF TABLES

This page intentionally left blank.

1. INTRODUCTION

Vertical-axis wind turbines (VAWTs) have been the subject of research and development for nearly a century [1]. However, this turbine architecture has fallen in and out of favor on multiple occasions. Beginning in the late 1970s, the U.S. Department of Energy sponsored an extensive experimental program through Sandia National Laboratories which produced a mass of experimental data from several highly instrumented turbines. Turbines designed, built, and tested include the 2 meter, 5 meter, 17 meter, and 34 meter and their respective configurations [2], [3], [4], [5] .This program kicked off a commercial collaboration and resulted in the FloWind turbines [6]. The FloWind turbines had several notable design changes from the experimental turbines that, in conjunction with a general lack of understanding regarding predicting fatigue at the time [7], led to the majority of the turbines failing prematurely during the late 80s.

More recently, interest has resurged for VAWTs for certain applications. Differing cost relationships for floating offshore wind energy and distributed wind systems relative to land-based utility wind systems can favor VAWT designs, due to reductions in support structure and maintenance costs. The vertical turbine's lower center of gravity, easy access to the drivetrain, and removal of active components (yaw and, in some cases, pitch systems) offer significant advantages for these concepts. While significant work has been done to understand and improve the aerodynamics of this architecture (a summary of over 70 articles can be found in the following book chapter [8]), aero-elastic modeling and especially validation has significantly lagged behind. This has been emphasized in several recent publications including [9] and [10]. Codes including floVAWT [11], HAWC-2 [12], Simo-Riflex-DMS [13], Simo-Riflex-AC [12], and Q-Blade [14] have had capabilities added to model vertical-axis turbines and are generally well validated for horizontal turbines, but gaps exist in the time-domain aero-elastic validation for vertical-axis architectures. The most complete known aero-elastic validation publication is the validation effort of Q-Blade against the Sandia 34m turbine [15] which goes as far as gravitational blade stress validation but which switches to code-to-code comparison for dynamic aero-elastic data. The current work extends beyond prior validation efforts by comparing the experimental and numerical blade strains and stresses in the unsteady domain for a variety of turbine operating cases.

Specifically, this paper will review the OWENS aeroelastic code, present the experimental validation data, and show simulation comparisons against a series of analytical cases and several experimental tests from the Sandia 34 meter turbine. The validation cases consist of multiple levels of cantilever beam analyses in addition to full turbine analyses, including modal, parked gravity loading, still air forced centrifugal loading, normal operation, and emergency shutdown. The ability to accurately model and design these complex flexible systems is critical to move beyond siloed theoretical physics into the coupled physically accurate domain that will enable commercial success.

This page intentionally left blank.

2. OWENS (OFFSHORE WIND ENERGY SIMULATOR)

The Offshore Wind ENergy Simulator (OWENS) was originally developed to meet the needs for design and simulation of VAWTs in 2013. The structural module solves the equations of motion for a gyric system in the rotating hub frame for ease of inclusion of centrifugal effects [16]. A beam finite element mesh is used to represent the rotor and elasticity and is solved through the use of Timoshenko beam elements [17]. Beyond the standard Timoshenko finite element formulation, OWENS includes VAWT-related considerations including gyroscopic, spin softening, centrifugal stiffening, and Coriolis effects. The structural model has been previously validated for modal resonant predictions, and had notable verification comparisons between the different modes of unsteady operation [17]. This code has been rewritten in the Julia programming language [18] and formulated to enable two-way coupled dynamic simulations necessary for design and optimization of floating vertical-axis wind turbines. The improved capabilities for OWENS includes; 1) Aerodynamic simulation using the Actuator Cylinder or Double Multiple Streamtube models in either one-way and two-way coupling with modeling and numerical improvements for simulating curved blades [19], 2) Translation into the Julia programming language, enabling significant speedup, automatic differentiation, and the ability to ship compiled binaries or shared libraries without extensive code modifications, 3) All of the necessary preprocessing including mesh generation, sectional property calculation, and data reformatting are now within a single automated module as opposed to multiple manual file-based operations, 4) The major components of the code have been modularized and are driven by a glue code which enables easy integration of alternate models. It should be noted that OWENS is not intended to be a high fidelity solver itself, but maintain a multidisciplinary level of speed and accuracy that enables efficient design and simulation of certification cases with an adequate level of accuracy. With that being said, we have modularized the code in such a way as to enable the coupling of high fidelity codes as future needs arise. The current major modules are as follows:

- OWENS: combines the modules into a continuous analysis workflow from basic parametric inputs to response outputs for steady, unsteady, and modal analyses. While it has been tuned for stability and accuracy, it also makes a wide range of fidelity and solution parameters/flags accessible to the user to enable use-case-specific tuning for accuracy and stability. This also includes the ability to modify control inputs for the full range of typical control elements.
- OWENSAero: consists of steady and unsteady analysis methods for 3D VAWTs (Double Multiple Streamtube and Actuator Cylinder), including dynamic stall models, multiple Reynolds/Mach/Family of airfoils lookup, and a new unsteady method (RPI) Rotating Point Iteration which enables faster than real-time aerodynamic simulations by reducing the required calculations to only the current blade positions as opposed to the entire cylinder of each vertical turbine slice. Additionally, the aerodynamic models were reformulated to properly account for curved blades which resolves a major source of error for Darrius configurations. This tool was verified against the Sandia CACTUS vortex solver [20] despite the relative simplicity and lack of virtual angle of attack corrections. Specific details on the formulation can be found in [19]. The OpenFAST [21] InflowWind library is optionally coupled to OWENSAero for turbulent inflow simulations.
- OWENSFEA: is a gyric beam finite element model built on Timoshenko elements. It consists of linear and nonlinear unsteady analysis, modal analysis with centrifugal stiffening, reduced order

model analysis (using mode shapes), and steady state analysis. While details on its formulation and limitations can be found in [17], It verifies well against geometrically exact beam theory even for moderate (20% of length) deflections as will be shown in this paper.

- OWENSPreComp: takes in general geometric and sectional composite layup inputs and generates a custom mesh and calculates sectional properties via NREL's OWENSPreComp [22] code (translated to Julia as well). While it does have the ability to output a full range of input files, it is designed for efficient direct coupling to the finite element solver's expected inputs.
- Simplified coupling to external modules for pre and post processing such as rainflow counting, classical lamination theory and failure, and simplified analytical buckling theory, in addition to geometrically exact beam theory for the structural solver.
- Additionally, direct coupling to the OpenFAST Hydrodyn and Moordyn modules have been done to enable floating platform simulations, which will be covered in a separate publication.

3. VERIFICATION AND VALIDATION

To verify and validate the OWENS code, we take a sequential approach which increases in complexity as is typically prescribed for a validation hierarchy [23]. Since the base elastic solution of the structural code was not previously verified, we start with simple analytical cases and use a geometrically exact beam theory code for code-to-code comparison [24]. These comparisons include cantilever and centrifugal deflection, modal analysis, and Campbell Diagram analysis in addition to unsteady harmonic forcing. After this brief verification to build confidence in the elastic solver, we transition to the more complex built-up Sandia 34m turbine structure. We conduct validation against experimental sectional properties, modal analysis, steady state gravitational and centrifugal loading, and a variety of unsteady 2-way aeroelastic performance cases with blade strain gauge data.

3.1. Structural Solver Verification

To validate the structural dynamics portion of the code, we begin by using a simple cantilever beam to verify modal predictions including centrifugal effects, steady state tip displacement, steady state centrifugal loads displacement, and dynamic response. The beam used is a simple rectangular cross section with fixed-free boundary conditions and no gravity loads, as depicted in the undeformed state in Fig. 3-1. Some of the comparisons also use a bent beam, which is the same as the straight beam, but with a 45 degree bend in the center, as shown in the undeformed state of Fig. 3-2b. The parameters used for the beam are shown in Table 3-1, while Eq. (3.1) and Eq. (3.2) give the sectional stiffness and mass matrices which are used for each element along the span.

Table 3-1. Simple cantilever beam definition.

Name	Value
length (L)	0.5 m
width (b)	0.05 m
height (h)	0.02 m
area (A)	0.001 m^2
elastic modulus (E)	210 GPa
poisson ratio (v)	0.28
shear modulus (G)	82.03 GPa
density (ρ)	7800 kg/m^3
moment of inertia (I_{yy})	3.33E-8 m^4
moment of inertia (I_{zz})	2.08E-7 m^4
torsional moment of inertia (J)	2.42E-7 m^4
tip load (P)	0:1e4:1e5 N
RPM	0:1e4:1e5 RPM
number of elements	40

$$\text{Stiffness Matrix} = \begin{bmatrix} E*A & 0 & 0 & 0 & 0 & 0 \\ 0 & G*A & 0 & 0 & 0 & 0 \\ 0 & 0 & G*A & 0 & 0 & 0 \\ 0 & 0 & 0 & G*J & 0 & 0 \\ 0 & 0 & 0 & 0 & E*I_{yy} & 0 \\ 0 & 0 & 0 & 0 & 0 & E*I_{zz} \end{bmatrix} \tag{3.1}$$

$$\text{Mass Matrix} = \begin{bmatrix} \rho*A & 0 & 0 & 0 & 0 & 0 \\ 0 & \rho*A & 0 & 0 & 0 & 0 \\ 0 & 0 & \rho*A & 0 & 0 & 0 \\ 0 & 0 & 0 & \rho*J & 0 & 0 \\ 0 & 0 & 0 & 0 & \rho*I_{yy} & 0 \\ 0 & 0 & 0 & 0 & 0 & \rho*I_{zz} \end{bmatrix} \tag{3.2}$$

3.1.1. Modal Analysis

The analytical expression for the natural frequencies (ω_n in rad/s) of the straight cantilever beam is shown in Eq. (3.3). The analytical correction factor k_n as described in [25] is 1.875 for the first mode, 4.694 for the second, and 7.855 for the third.

$$\omega_n = \sqrt{\frac{E*I_{yy}}{\rho*A}} * \left(\frac{k_n}{L}\right)^2 \tag{3.3}$$

Table 3-2 gives the resulting modal frequencies and relative error, all of which are less than 1.63%. Note that while not shown, the mode shapes also match well. We also introduce GXBeam.jl [26] a previously verified an validated geometrically exact beam theory based on the open source GEBT code [24] and related publications [27] [28]. Geometrically exact beam theory is an efficient and accurate substitution for 3-D structural analysis, and GXBeam itself offers additional advantages being written in the Julia programming language with minimal overhead and employing methods for built up structures, unsteady analysis, and modal simulation. We use GXBeam for code-to-code comparison in later analyses as needed, in addition to using it as an optional alternative to the Timoshenko beam elements within the OWENS dynamic simulations. We include comparisons here against the analytical test cases to build confidence for the more complex analyses which do not have analytical solutions.

Table 3-2. Simple cantilever beam modal results.

Mode	Analytical (Hz)	OWENS (Hz)	OWENS Error (%)	GXBeam (Hz)	GXBeam Error (%)
1	67.05	66.98	0.11	66.99	0.09
2	420.21	417.17	0.72	418.02	0.52
3	1176.72	1157.48	1.63	1163.03	1.14

3.1.2. Tip Deflection with Tip Point Load

We now use the same straight beam but look at the tip deflection from a constant tip load. The analytical expression [29] is shown in Eq. (3.4). Table 3-3 gives the resulting tip deflection and relative error; we again

include GXBeam results to build confidence. Note that the analytical expression is linear while OWENS and GXBeam are able to run in both linear and nonlinear modes.

$$\delta_i = \frac{P_i L^3}{3EI_{yy}} \tag{3.4}$$

Table 3-3. Simple cantilever beam linear tip deflection for three sample load results.

Load (N)	Analytical (m)	OWENS (m)	OWENS Error (%)	GXBeam (m)	GXBeam Error (%)
1E4	0.0595	0.0595	0.045	0.0593	0.101
5E4	0.298	0.297	0.045	0.298	0.101
1E5	0.595	0.595	0.045	0.596	0.101

Figure 3-1 gives a visual representation of both nonlinear and linear beam shapes under load. Since the deflection is greater than 20% of the beam length, the fundamental assumptions of the Timoshenko formulation begin to be violated and the solutions begin to differ. For this case, there is a 3.26% difference in the nonlinear tip deflection while the linear solutions are nearly identical with error less than 0.101%. Also note that OWENS is formulated to use only follower forces, which are forces applied that maintain the orientation relative to the beam regardless of the beam's deflected state. Follower forces were used in GXbeam for consistency between the two models.

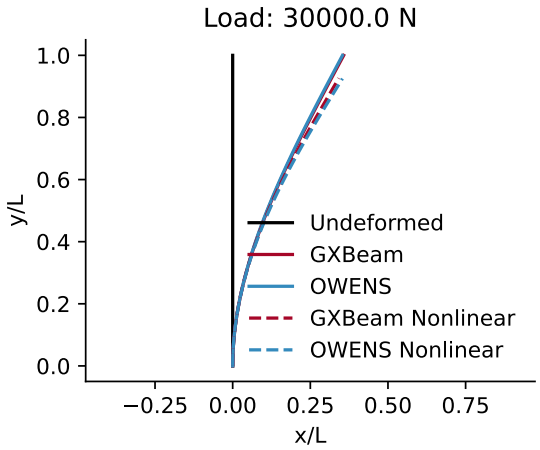

Figure 3-1. Straight beam deformed mesh for both linear and nonlinear analysis up to 30% tip deflection compared to length.

3.1.3. Centrifugal Force Deflection

Modeling a spinning beam with a bend exercises the ability to predict centrifugal effects on multiple structural degrees of freedom. The beam tested is the same as the previous examples, but with a 45 degree bend in the middle. Figure 3-2a shows the beam shape and an example deflection for relatively high RPM for both linear and nonlinear analysis. Rotation is about the z-axis or out of the page around the fixed end. This case, in addition to the tip deflection at varying RPM (Fig. 3-2b), shows excellent agreement between the two codes with similar error as the straight beam tip deflection.

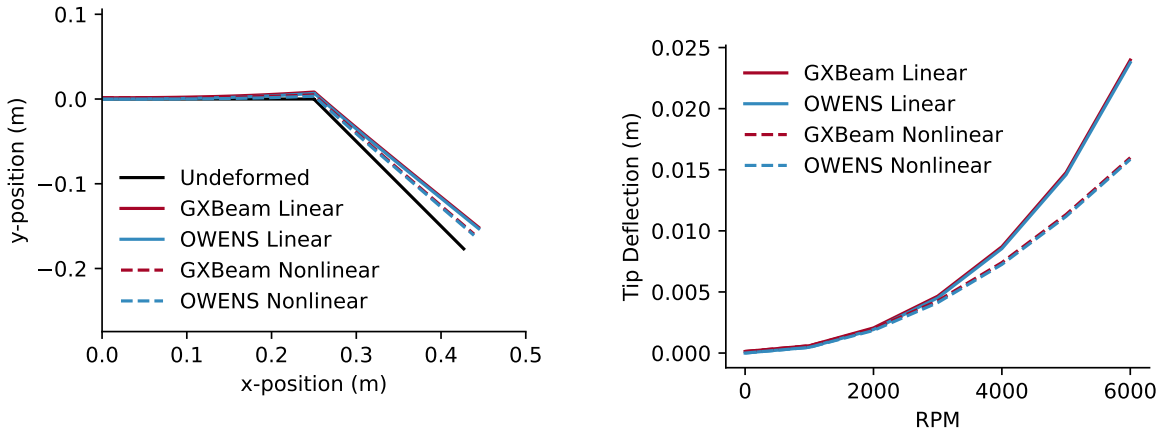

(a) Example geometry and deflection at 6000 RPM with excellent agreement.

(b) Tip deflection for varying RPM levels with excellent agreement.

Figure 3-2. Bent cantilever beam deflection undergoing rotation about the z axis (out of the page).

3.1.4. Modal Analysis with Centrifugal Stiffening

A spinning beam which undergoes significant deformation experiences centrifugal stiffening which in turn affects the natural frequencies. Accurate prediction of this phenomenon is important for large wind turbines as the rotating modal frequencies can overlap with the blade pass forcing frequencies in operation. Figure 3-3 shows the resulting Campbell diagram of the spinning beam with a bend and reveals excellent agreement between the two codes for the lower frequencies, and a maximum 2.8% error for the 6th mode, a relatively complex coupled bend-twist torsional mode with three neutral points. Despite the complexity of the higher order modes, the two codes match well for the mid-level fidelity of the tools.

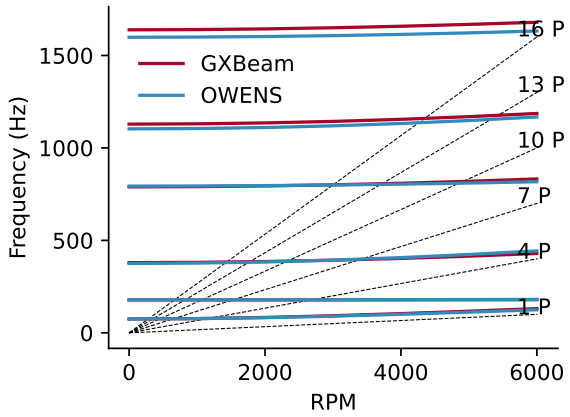

Figure 3-3. Campbell diagram analysis of the bent cantilever beam undergoing rotation about the z (out of the page) axis.

3.1.5. Unsteady Tip Forcing

The test cases so far have been for static or steady state analyses. To test the dynamic response, we switch beam properties to enable more apparent harmonic frequency excitement. However, the damping models between the two codes differ appreciably enough to make finding a relationship challenging. GXBeam applies the damping coefficients directly to the strains while OWENS applies them to the internal damping matrix. For this verification, if we were to manually tune the damping coefficients, the solutions can be made to match within 5% error. However, in light of these challenges, we simply use the same damping values for both models and focus on the qualitative nature of the harmonic forcing. In the following sections against the full turbine, the harmonic forcing outputs are discussed and shown in more detail.

For this case, we use a straight beam with 20 elements and the properties given in Eqs. (3.5) and (3.6). We apply a sinusoidal forcing to the tip of -1e5*sin(20*t) ([27]). Additionally, damping coefficients of 0.005 were applied to both OWENS alpha and beta Rayleigh terms and to each of the six degrees of freedom for each node in GXBeam. This value was chosen to allow for resonance without allowing the high frequency content to dominate the solution.

$$\text{Mass Matrix} = \begin{bmatrix} 258.035 & 0.0 & 0.0 & 0.0 & 0.0 & 0.0 \\ 0.0 & 258.035 & 0.0 & 0.0 & 0.0 & 0.0 \\ 0.0 & 0.0 & 258.035 & 0.0 & 0.0 & 0.0 \\ 0.0 & 0.0 & 0.0 & 48.59 & 0.0 & 0.0 \\ 0.0 & 0.0 & 0.0 & 0.0 & 2.172 & 0.0 \\ 0.0 & 0.0 & 0.0 & 0.0 & 0.0 & 46.418 \end{bmatrix} \tag{3.5}$$

$$\text{Stiffness Matrix} = \begin{bmatrix} 2.389E+09 & 0.0 & 0.0 & 0.0 & 0.0 & 0.0 \\ 0.0 & 4.334E+08 & 0.0 & 0.0 & 0.0 & 0.0 \\ 0.0 & 0.0 & 2.743E+07 & 0.0 & 0.0 & 0.0 \\ 0.0 & 0.0 & 0.0 & 2.167E+07 & 0.0 & 0.0 \\ 0.0 & 0.0 & 0.0 & 0.0 & 1.970E+07 & 0.0 \\ 0.0 & 0.0 & 0.0 & 0.0 & 0.0 & 4.406E+08 \end{bmatrix} \tag{3.6}$$

The resulting base loads are shown in Figs. 3-4 to 3-6. The damped natural frequency of the solution matches and despite the difference in damping formulation, the root mean square values vary by 32%, 16%, and 9% for the three comparison loads. Increasing the damping coefficients produces a similar level of agreement between the two models, but with attenuated amplitude and frequency as expected. From a qualitative assessment, this analysis shows the code ability to model unsteady resonance due to periodic loading and if a relationship between the two codes' damping models was developed would match within the level of accuracy demonstrated in the other cases.

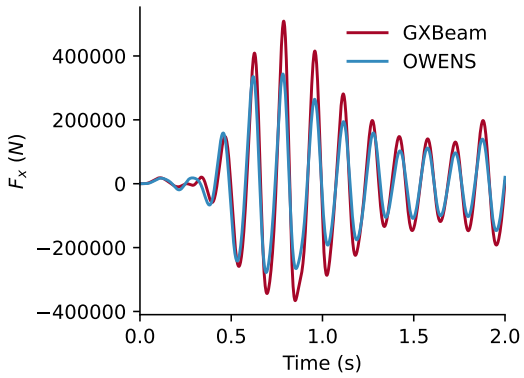

Figure 3-4. X-direction reaction force at the beam root.

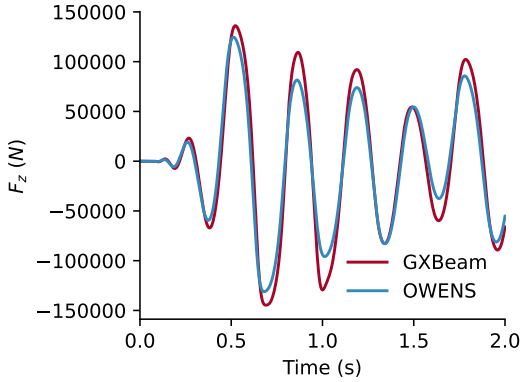

Figure 3-5. Z-direction reaction force at the beam root.

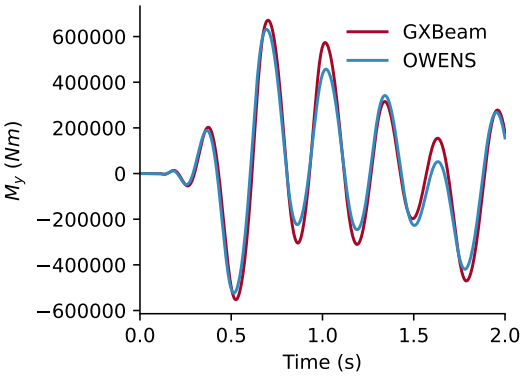

Figure 3-6. Reaction moment about the Y-axis at the beam root.

3.2. SNL 34m Structural Validation

Vertical-axis turbine experimental campaigns at Sandia National Laboratories extended over a period of nearly two decades, culminating with the design and testing of a highly instrumented 34 meter diameter VAWT (see Fig. 3-7). More specific details than are given here are contained in [5]. In summary, this turbine had two blades, rigid blade mounts, and top-mounted guy wires for support. The blades were comprised of three unique blade sections as depicted in Fig. 3-8b, and made of 6065-T6 aluminum. The overall geometric dimensions of each blade section, its chord, and respective airfoil section can be seen in Fig. 3-8a.

Figure 3-7. Sandia 34 meter VAWT in Bushland, Texas. Photo used with permission from Sandia National Laboratories.

There were distributed strain gauges along the turbine blades which were used to measure the blade response to parked gravitational loads, forced centrifugal loads, and a variety of unsteady operational loads. The majority of the time-domain data that were preserved in technical reports focuses on the upper and lower root sections of the turbine, where the loads tend to be the highest. The remaining data were recorded in statistical values as will be discussed in later sections.

The Sandia 34m turbine blades were constructed in three sections as shown in Fig. 3-8. As the most fundamental starting point to validate the SNL 34m structural response, we compare the experimental sectional properties [30] to the calculated properties in Table 3-4. Calculated properties are computed from from OWENSPreComp [22], approximating the aluminum skin and shear webs as lamina to comply with the expected composite layup inputs. The tower was comprised of a simple aluminum tube 3 meters in diameter and 12.5 mm thick. The resulting blade properties match within less than 1.5% for all of the values except the outer or root lag stiffness with a reasonable 3.53%. A possible explanation for the added error could be the increased number of joints for that extrusion since the sections were extruded in multiple parts and joined. This would make the simulated section slightly stiffer since there would be no slipping in the joined areas.

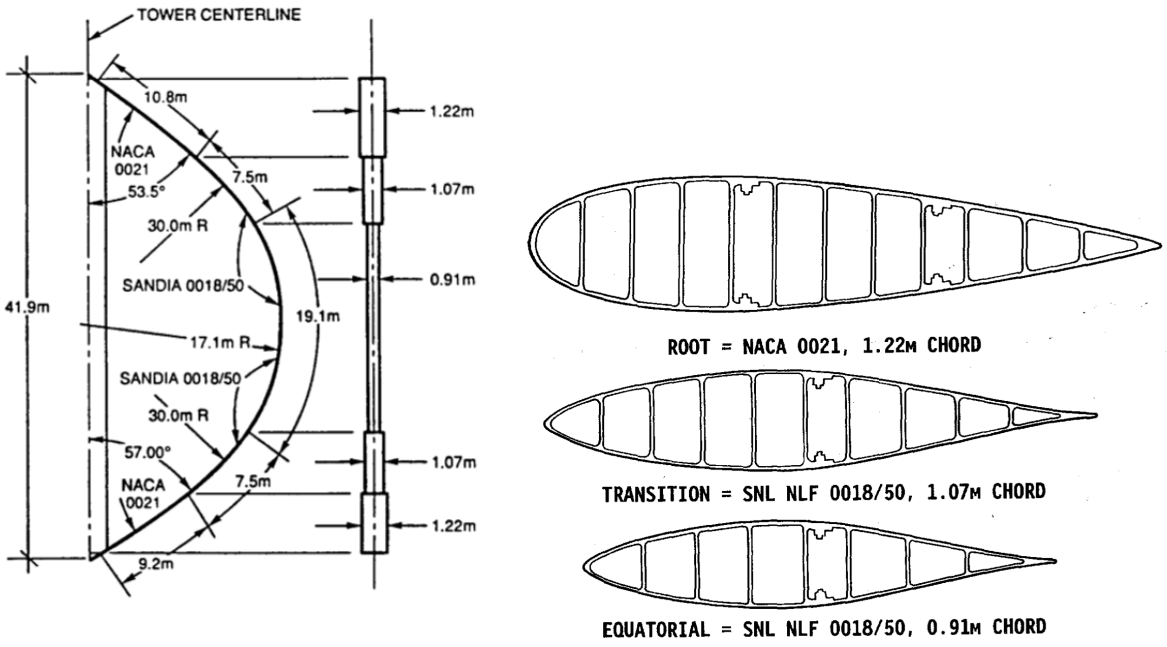

(a) Turbine Geometry. **(b) Sectional Geometry.**

Figure 3-8. Sandia 34 meter shape definitions. Images to scale.

Table 3-4. Comparison of Blade Sectional Properties.

Section	EA			EI Flap			EI Lag		
	Exp.	OWENS	Error (%)	Exp.	OWENS	Error (%)	Exp.	OWENS	Error (%)
Outer	2.632e9	2.599e9	1.25	1.649e7	1.674e7	1.52	2.744e8	2.841e8	3.53
Mid	1.478e9	1.498e9	1.38	5.197e6	5.267e6	1.36	1.125e8	1.130e8	0.42
Inner	1.185e9	1.201e9	1.32	3.153e6	3.195e6	1.32	6.674e7	6.762e8	1.32

3.2.1. Campbell Diagram for the 34m

Using the blade and tower properties, we construct an accompanying OWENS mesh and run modal analyses with successively increasing RPM to create a Campbell diagram. The mesh is comprised of independent tower, blades, and the root fasteners, which were modeled as shallow struts. The root fasteners have the same properties as the blade base sections. These sections are combined via rigid joints to create the rotating structure. OWENS solves in the rotor frame of reference, and so the bottom node is fixed in all degrees of freedom and the top is fixed in planar and vertical translation to represent the effect of the upper guy wire supports on the test turbine. Figure 3-9 shows the response of both GXBeam and OWENS against the experimental data. The experimental turbine did not have a truly fixed top but was rather constrained by guy cables. The first tower mode in the presence of the cable pretension and stiffness is identified in Fig. 3-9 and would be captured if elements were added to the mesh that approximated the spring-like nature of the cables. However, the predicted blade modes do not differ appreciably.

The results between OWENS and GXBeam match well as expected considering the same mesh and structural properties were used. At higher RPM, as deflections and nonlinear differences increase, the solutions begin to differ, with a maximum percent difference of 5% at 40 RPM for the second blade mode. Compared to the experimental data, there are notable differences in the higher RPM areas (as much as 17% for the highest RPM and blade mode), however, the parked (0 RPM) cases differ by less than 8%. Of the many sources of uncertainty associated with the experimental data and numerical analysis conducted, the greatest note may be the lack of simulated aerodynamic interactions while spinning. The strain stiffened modal analyses conducted in both OWENS and GXBeam only include centrifugal forcing. Adding this capability to the code may lower the simulated frequency of some of the higher frequency modes at higher RPM levels. Additionally, the uncertainty associated with the differences in blade sectional properties already reviewed, where the simulated properties are slightly stiffer, may also contribute to the general offset towards higher modal frequencies.

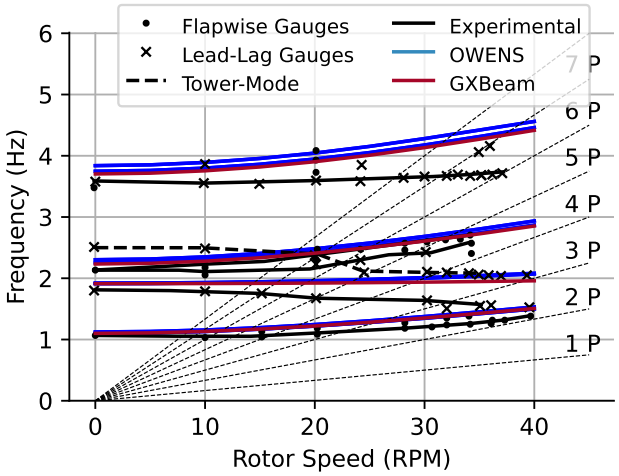

Figure 3-9. Campbell diagram of the 34 meter turbine showing strain gauge measurements, OWENS, and GXBeam predicted frequencies.

3.2.2. Static Gravity Loads

During construction of the turbine, the blade instrumentation was zeroed in a relaxed ground state prior to mounting the blades. Once the blades were mounted, the strain was recorded, which captures the gravity loads. In the experimental data, a simplified stress was reported, which was the measured surface strain multiplied by the material modulus of elasticity. Figure 3-10 shows the experimental and predicted gravity loads showing good agreement in magnitude and form with some under-prediction at the 35 meter span position. The original report [30] included predicted loads from finite element analysis which also under-predicted the stress at this location. It is possible that some error was introduced due to the difficult nature of getting such large blades to be in a neutral state while on the ground.

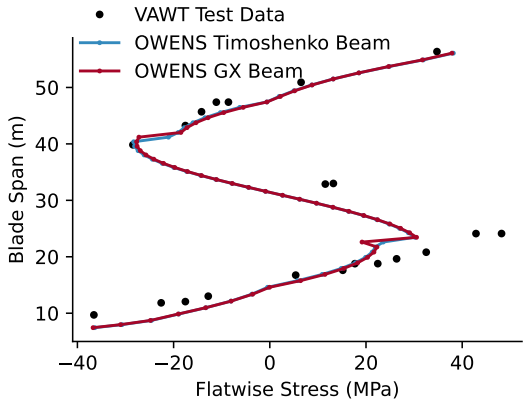

Figure 3-10. Gravity loads showing longitudinal stress along the blade.

It should also be noted, that to model subsequent tests, we must follow the experimental procedure of zeroing out the gravity loads. Numerically, this means we need to run simulations with gravity and subtract the gravity-only loads. This is necessary to achieve the correct deformed blade shape under centrifugal loads and gravity since the centrifugal stress is very sensitive to the final deformed blade shape.

3.2.3. Still Air Centrifugal Loads

With the gravity loads known, we can run the still air centrifugal load cases. This is simply done by running a simulation with zero windspeed, but with the two-way aerodynamic model active to capture the drag forces on the blades. Figure 3-11a shows the resulting centrifugal stresses at 28 RPM and Fig. 3-11b at 40 RPM. Both cases show excellent agreement across the blade span.

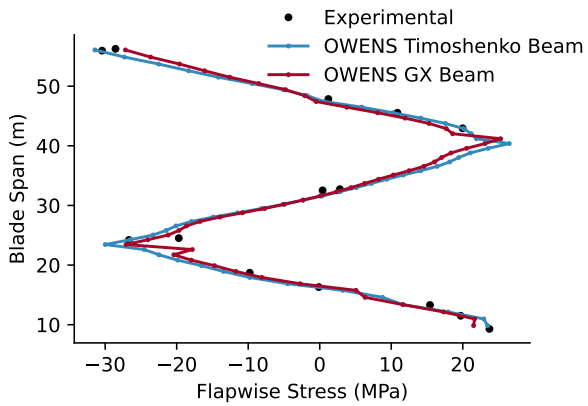

(a) 28 RPM forced spinning (calm wind) centrifugal stresses.

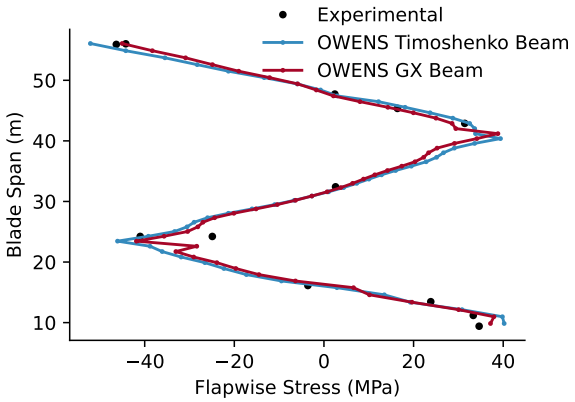

(b) 40 RPM forced spinning (calm wind) centrifugal stresses.

Figure 3-11. Centrifugal blade loads comparison.

3.2.4. Blade Shape and Centrifugal Stress Sensitivity

It should be noted that there is a very high sensitivity to the blade shape and centrifugal stress. When we compared the original drawings to digitized photographs of the 34m blade shape, we found as much as a 2.13% difference in blade shape (relative to the turbine diameter). While this is relatively small and has a negligible effect on the gravity stress, it has a large effect on the centrifugal stresses.

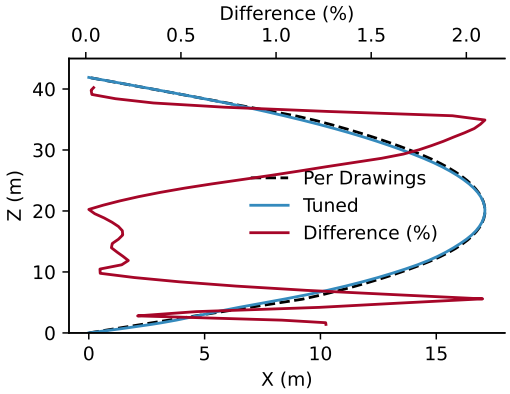

(a) SNL 34m blade shape, difference between shapes is less than 2.13% of the turbine diameter.

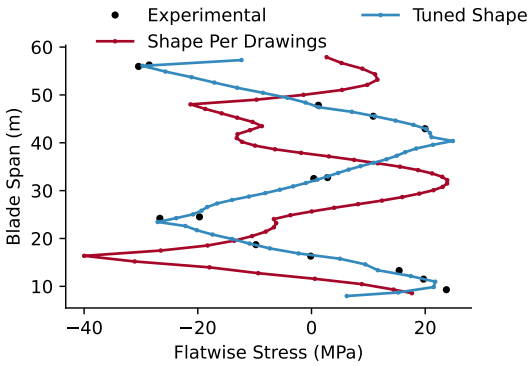

(b) 28 RPM centrifugal stress variation due to blade shape.

Figure 3-12. Sensitivity of blade shape on centrifugal loads.

Simply using the shape as given in the drawings, or the shape from legacy photos gives an overall trend of increasing and decreasing loads, similar to the experimental, but without general alignment and agreement. Due to this difference and sensitivity, we tuned the shape as shown in Fig. 3-12a within the known uncertainty

to achieve a more realistic simulation, which is used in the analyses for this report. Figure 3-12 shows the relative difference between the shape per the drawings, and the tuned shape that was used.

3.3. SNL 34m Steady State Aeroelastic Performance Validation

Up to this stage, loads and deformations have not included coupled aerodynamic considerations. Before presenting aerostructurally coupled results, we give a high level overview of the aerostructural coupling. There are four modes: no aerodynamic coupling, rigid aerodynamics, partial coupling where the deformation from the last timestep is used to deform the aerodynamics for the current time step, and full two way coupling where the aerodynamics and structures are iterated on at each time step until convergence, exchanging loads and deformations between the two models. Verification and validation of the aerodynamics solver alone has been previously published [19] so we primarily focus on the aeroelastic validation here. Of note is that the Boeing-Vertol dynamic stall model was used with 360 degree extrapolated Sandia and NACA airfoils and no virtual angle of attack corrections, tower shadow, or strut modeling was used.

Overall turbine performance is generally characterized by the coefficient of performance (CP) which is derived from torque. For a turbine operating at constant RPM, such as the Sandia 34m turbine operating at 34 RPM, high tip speed ratios occur at low wind speed and have low torque values, which lead to a higher level of error in experimental torque sensor outputs. For example, if the torque sensor has an uncertainty of 1% at its peak value of 150 kN-m, then a torque value of 15 kN-m would have an uncertainty of 10% and so on. This means that while the absolute errors shown in the left side of Figure 3-13b are small, when converted to CP, the relative errors are much higher as shown on the corresponding right side of Fig. 3-13a. The maximum error for torque occurs in the low TSR, high wind speed regions, where the turbine is operating under significant variations in angle of attack and the dynamic stall models are active. This maximum error is approximately 15% on the torque predictions. Of note is that the design operating tip speed ratios for this turbine are between 3 and 6, for which there is low error for both CP and torque in both the experimental values and numerical simulation.

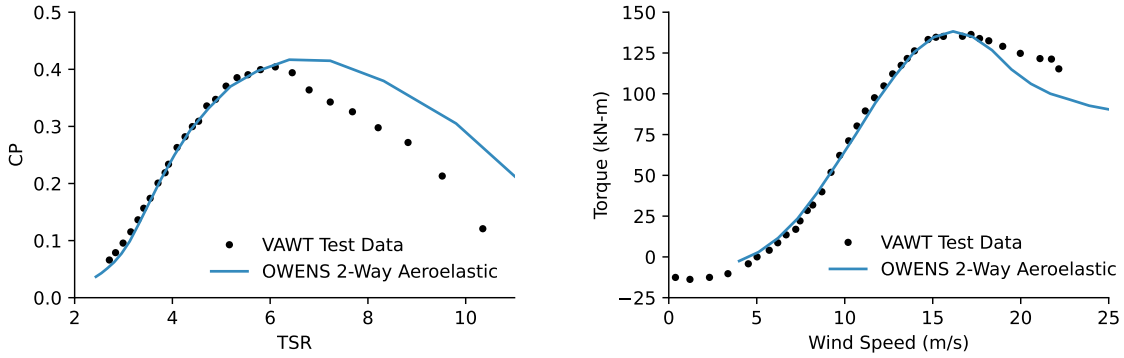

(a) Power Coefficient vs. Tip Speed Ratio **(b) Torque vs. Windspeed**

Figure 3-13. Performance comparison for the Sandia 34 meter turbine operating at 34 RPM comparing experimental and 2-way aeroelastic coupling.

3.4. SNL 34m Dynamic Aeroelastic Validation

With the overall turbine loads validated, we now move to the dynamic aeroelastic validation. The Sandia 34 meter test campaign recorded and retained time-history data for startup, normal operation, normal stop, and emergency stop at the root sections of the blade. OWENS has the ability to employ user-specified torque controls or directly specified RPM, with or without an active drivetrain spring-mass-damper model. The physical drivetrain system, as depicted in Fig. 3-14, included a purposefully compliant drivetrain via rubber isolators to attenuate the periodic blade-pass torque fluctuations by as much as 95%. The compliant drivetrain allowed the turbine to operate with an azimuthally varying RPM, which in turn changes the blade stresses. However, we have found that for this turbine, the change in blade stresses is small (less than 10%) and therefore either control method can be used as long as the compliant drivetrain model is active. For the normal operation case, we recreate the compliant drivetrain model and implement a simple PI controller to mimic the synchronous generator at normal operating conditions. The PI coefficients were calculated based on a regression fit from experimental RPM and torque during normal operation. For the other cases shown, the control logic could not be distilled as easily from experimental data and was not documented in the available documentation. To still enable a comparison on loads, we used the specified RPM method to run the simulated turbine at the time-varying experimental RPM.

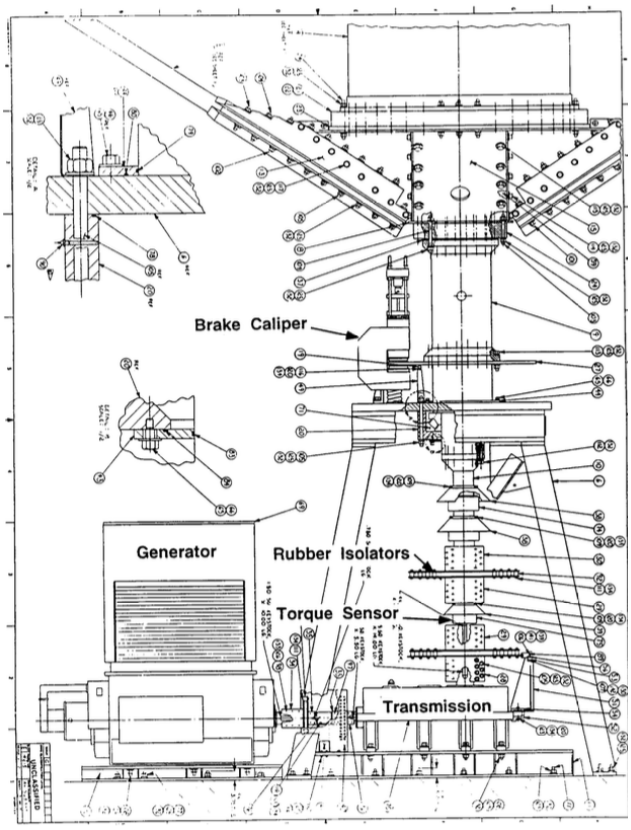

Figure 3-14. Sandia 34 meter turbine drivetrain.

3.4.1. Normal Operation

For normal operation, we recreated the drivetrain model and synchronous generator PI controller. Since the exact specifics of the design was not available at the time of writing, we used approximate values specified

in Table 3-5. We first ran the simulation for 20 seconds with unchanging inputs to achieve steady state, and then supplied the measured windspeed uniformly across the rotor. Figure 3-16 shows a the normal operation torque. Despite the uncertainties in modeling and initial conditions, the macro torque variations are in line with the varying wind speed at the site. Some error is also introduced since the windspeed was measured at a single point adjacent to the turbine at the turbine equator as shown in Fig. 3-15.

Table 3-5. Approximate drivetrain and driveshaft properties used for recreation of the 34m normal operation performance simulations.

Drivetrain Inertia	250.0 kg m2
Driveshaft Stiffness	10000 Nm/rad
Driveshaft Damping	1500 Nm/rad2
Torque Control Law	$Q_0 + K_p * RPM + K_i *$ Integral Error
K_p	10.63
K_i	5.26
Q_0	-320.15

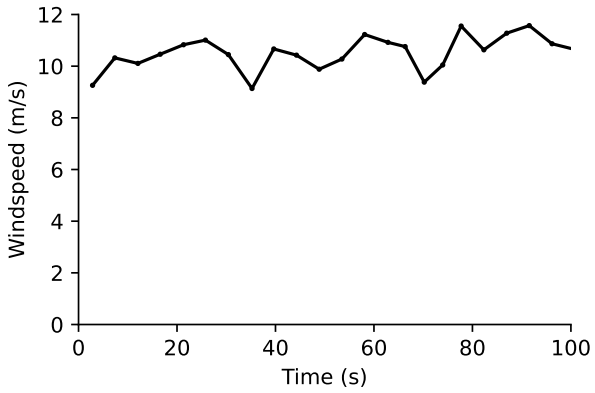

Figure 3-15. Recorded wind speed for the normal operation 34 RPM case.

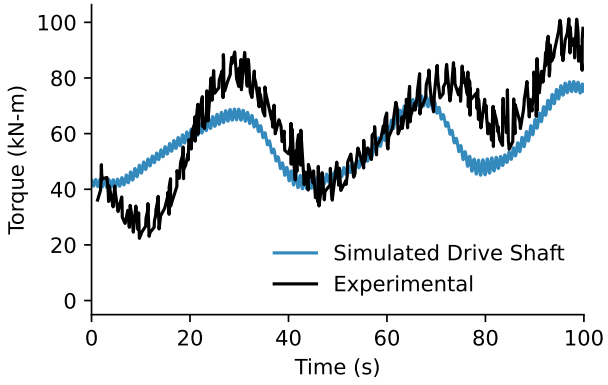

Figure 3-16. Turbine normal operation torque at 34 RPM.

Figures 3-17 and 3-18 show the flapwise and lead-lag simple stresses at the lower blade root. The strain gauges on the 34m turbine were installed in pairs, enabling pure bending moments to be measured, which is modeled in the simulated results. The flapwise strain gauges were installed at the thickest portions of the symmetric airfoil, and the lead-lag strain gauges were installed effectively at the leading and trailing edges. The lead-lag stress was calculated based on the distance from the neutral axis to the trailing edge. The mean loads differ by less than 5% for flapwise and less than 15% for lead-lag, and peak to peak loads differ by less than 15% for flapwise and 12% for lead-lag. The ability of the efficient low to mid-fidelity DMS aerodynamics coupled with the Timoshenko beam elements to predict aeroelastic loads to this level of accuracy is groundbreaking for commercial turbine design and certification.

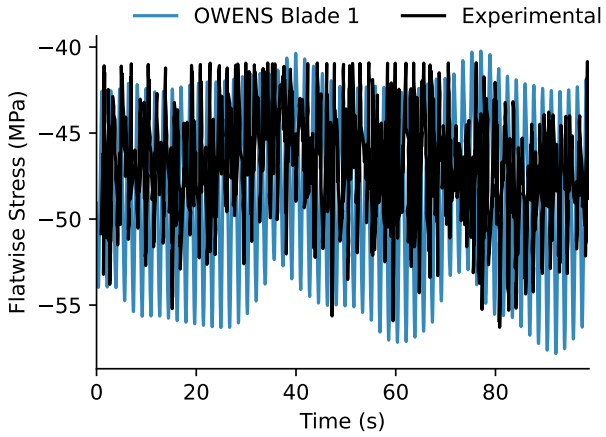

Figure 3-17. Turbine upper root normal operation flapwise stress at 34 RPM

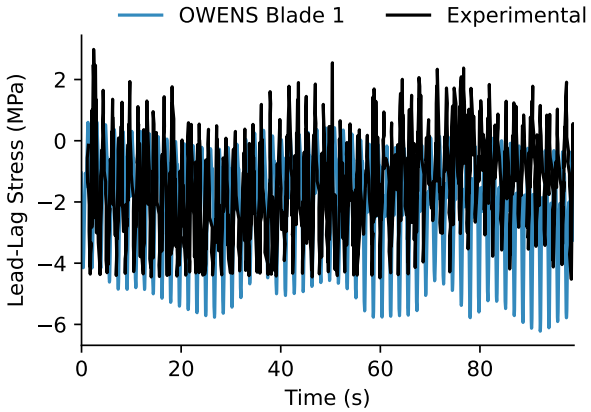

Figure 3-18. Turbine upper root normal operation lead-lag stress at 34 RPM

3.4.2. Emergency Stop

Emergency stop was modeled by running OWENS in the pre-specified RPM mode with the recorded RPM and windspeed as shown in Fig. 3-19. Figures 3-20 and 3-21 show the flapwise and lead-lag simple stresses. They show good agreement in the dynamics of stopping for both the mean and varying loads at the beginning, but deviate in the varying loads once the turbine RPM is significantly reduced. It is possible that a reduction in structural damping is needed depending on centrifugal loading.

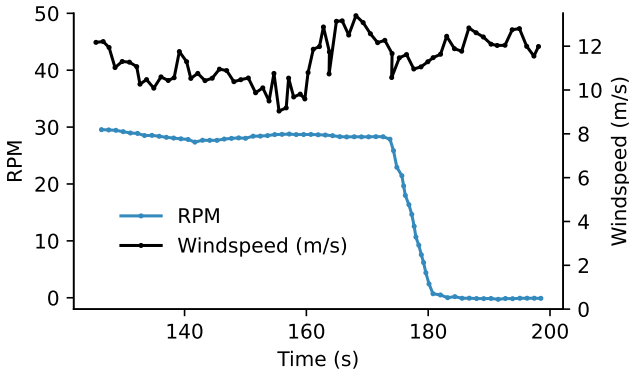

Figure 3-19. Turbine emergency stop used RPM and wind speed.

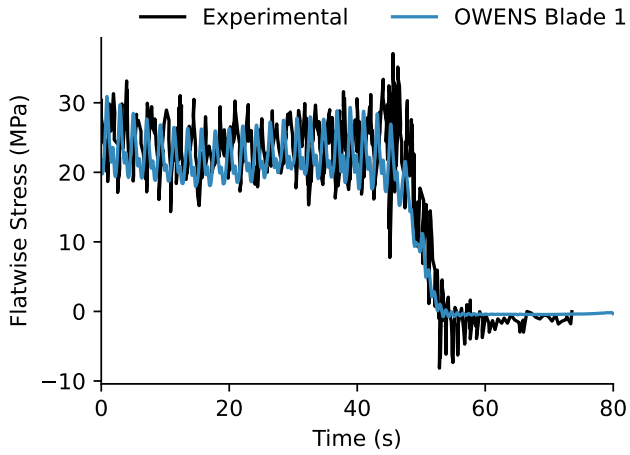

Figure 3-20. Turbine emergency stop lower root flapwise stress.

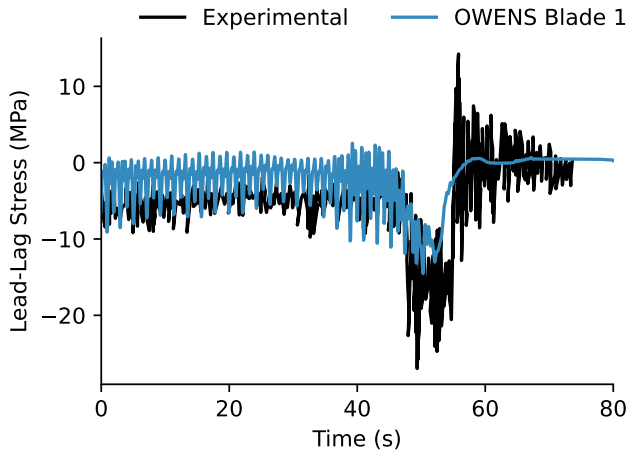

Figure 3-21. Turbine emergency stop lower root lead-lag stress.

3.4.3. Root Mean Variance

Though the 34m VAWT test campaign collected vast amounts of time data, the majority was summarized into what was termed the root mean variance, or RMV. This value is equivalent to the root mean square, but with the mean signal subtracted, and represents the principal oscillatory stress. The equation is summarized in Eq. (3.7).

$$\text{RMV} = \sqrt{mean\left(\left(\text{signal} - mean(\text{signal})\right)^2\right)} \tag{3.7}$$

In the original report [5], summary data is given for each active strain gauge location for both blades at varying wind speed, and at 28, 34, and 38 RPM. For the purposes of this paper, we show only a few key summary positions and discuss their impact. Namely, we show the upper and lower root, equator, and upper and lower quarter span locations. Figure 3-22 gives a visual location of the strain gauge A-Q locations.

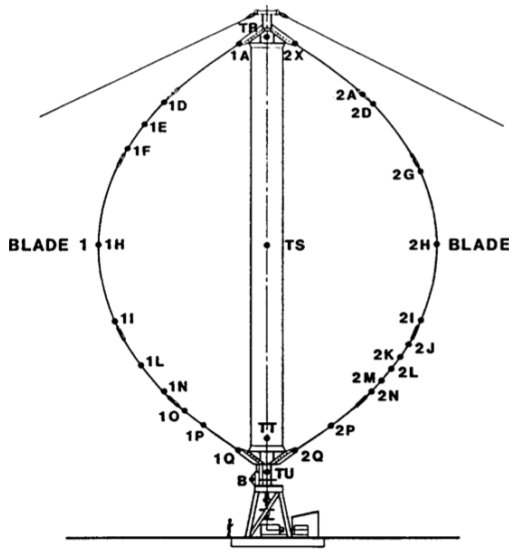

Figure 3-22. Sandia 34 meter turbine strain gauge locations.

To most accurately model the inflow conditions, we used TurbSim [31] to generate a class C normal turbulence model (NTM) intensity flow field with a 0.05 second timestep for each of the wind speeds. This is in accordance with the closest known atmospheric conditions, which are at the Sandia SWiFT facility [32]. While we use this turbulence model, there remains a significant amount of uncertainty in the actual turbulent inflow conditions during the experimental campaign, which should be taken into consideration when evaluating the differences between experimental and simulated results. In order to maintain steady state control of the turbine during the wide range of wind speeds, the generator control gains were scaled with the wind speed squared divided by 10.0 m/s squared (the original controller's design wind speed), in line with the standard wind turbine torque coefficient equation. The drivetrain model was unchanged. In the following plots, we divide both the experimental and simulated values by the simulated mean to give a relative comparison of the varying loads to the mean. The gauge identifier codes are interpreted as follows: the first character is the blade number, the second is the gauge location (A-Q), the third is the type of strain measured (bending moment - M, axial - A), and the fourth is the direction (flapwise - F, lead-lag - L). For example, the 1AMF gauge is for blade 1, location A, moment, in the flapwise direction. The only deviation

from this is the 1HF1 gauge, which was a backup gauge configured to measure flapwise moment at the H location.

Figures 3-23 to 3-27 show the upper root, upper quarter, equator, lower quarter, and lower root positions respectively. Overall there is good agreement in both flapwise and lead-lag loads with the percent RMV stresses aligning within 1% for flapwise stresses and within 2% for lead-lag stresses above 7.5 m/s wind speed with two exceptions. The first exception is the equator flapwise gauge (Fig. 3-25a) with a 2% level, which may be attributed to the backup gauge being used. The second exception is the lower lead-lag quarter location (Fig. 3-26b), which remains below 5% for experimental, which may be attributed to experimental uncertainty. For all of the lead-lag loads, the percent at wind speeds lower than 7.5 m/s increases due to the percent normalization where the RMV stress is much smaller compared to the mean, which amplifies small differences.

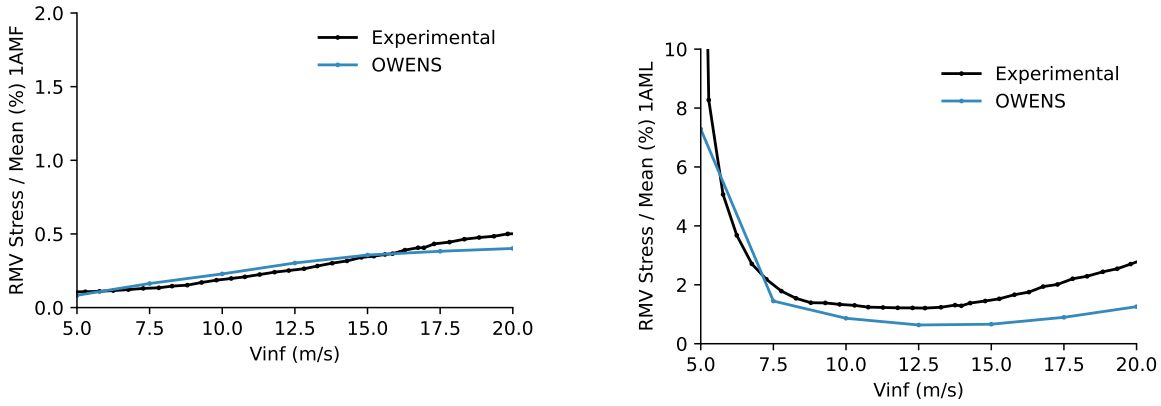

(a) Blade upper root flapwise RMV stress **(b) Blade upper root lead-lag RMV stress**

Figure 3-23. RMV stress percent of mean at the turbine upper root lag (1AMF) and flap (1AML) gauges at 34RPM with varying turbulent inflow velocity.

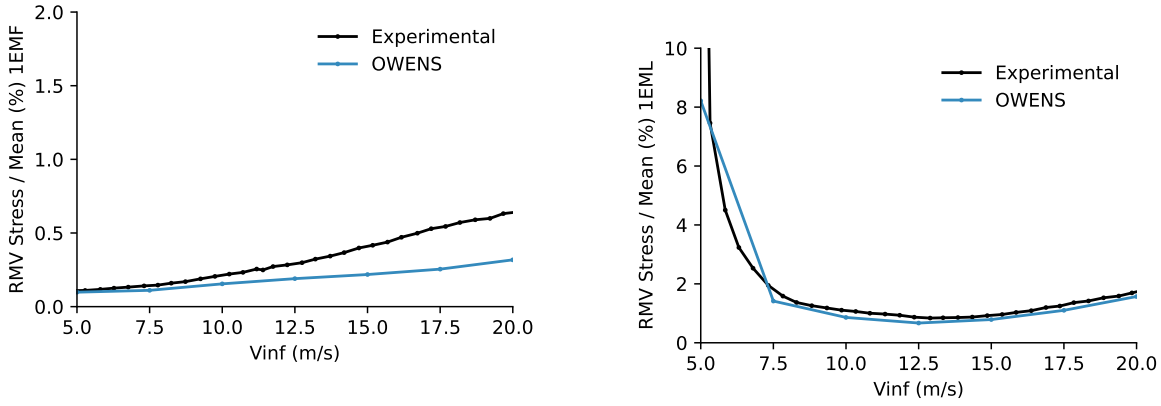

(a) Blade top quarter flapwise RMV stress **(b) Blade top quarter lead-lag RMV stress**

Figure 3-24. RMV stress percent of mean at the turbine upper blade quarter lag (1EMF) and flap (1EML) gauges at 34RPM with varying turbulent inflow velocity.

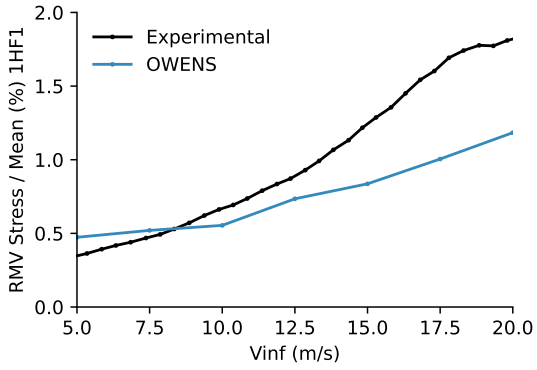

(a) Blade equator flapwise RMV stress

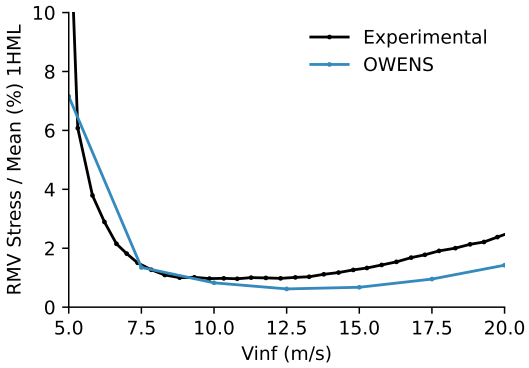

(b) Blade equator lead-lag RMV stress

Figure 3-25. RMV stress percent of mean at the turbine equator lag (1HF1) and flap (1HML) gauges at 34RPM with varying turbulent inflow velocity.

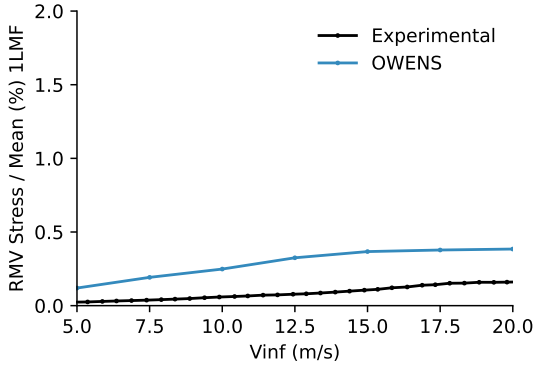

(a) Blade lower quarter flapwise RMV stress

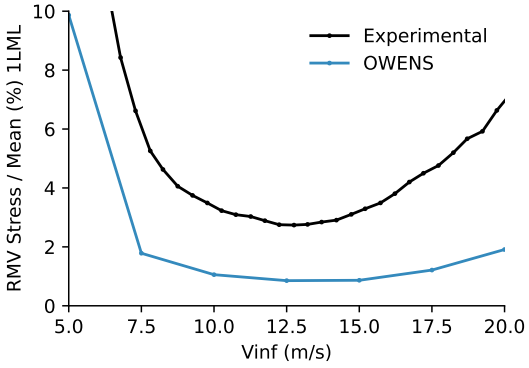

(b) Blade lower quarter lead-lag RMV stress

Figure 3-26. RMV stress percent of mean at the turbine lower quarter lag (1LMF) and flap (1LML) gauges at 34RPM with varying turbulent inflow velocity.

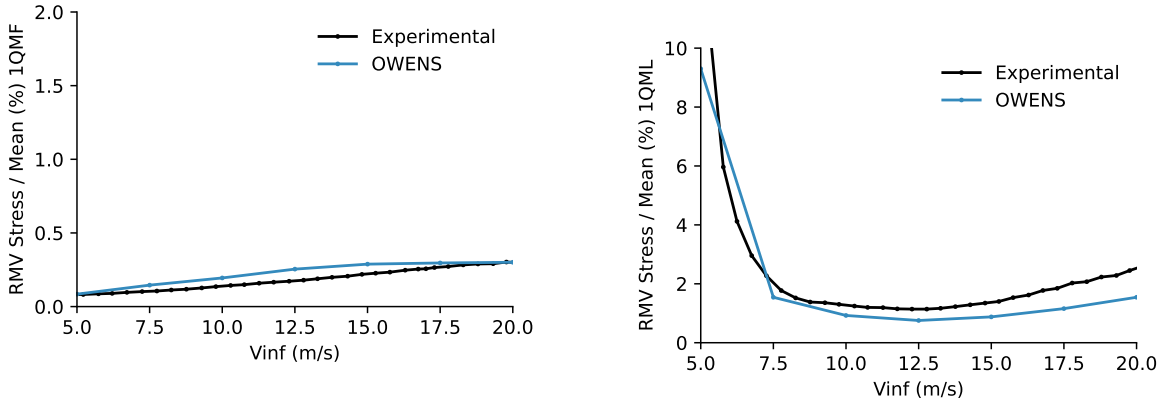

(a) Blade lower root flapwise RMV stress

(b) Blade lower root lead-lag RMV stress

Figure 3-27. RMV stress percent of mean at the turbine lower root lag (1QMF) and flap (1QML) gauges at 34RPM with varying turbulent inflow velocity.

This page intentionally left blank.

4. CONCLUSIONS

A comprehensive validation hierarchy for aeroelastic predictions of vertical-axis wind turbines has been developed based on increasing complexity of analysis from simple structures with analytical solutions to an unsteady time domain simulation of a 500 kW VAWT. Predictions have been performed with the OWENS aero-servo-elastic design tool and compared to analytical solutions, to predictions using a geometrically exact beam theory model, and to experimental data from the legacy Sandia 34 meter VAWT testbed. Based on the set of validation cases presented, OWENS has been demonstrated to be able to predict the modal performance including rotational effects and the gravitational, centrifugal, and two-way aeroelastically-coupled dynamic turbine loads with turbulent inflow. The relative discrepancies between the experimental and predicted values have been reviewed and the analysis sensitivities discussed.

In a simple cantilever beam case, we validated performance with the analytical resonance predictions and linear tip deflections with differences less than 2%. We found excellent agreement with the higher-fidelity geometrically exact beam theory (GEBT) model for non-linear model operation with deflections up to 30% of the beam length where over-predictions were less than 3.3%. For modal, a maximum of 2.8% difference in the 6th mode of a rotating bent beam was observed, which could be attributed to the challenges associated with capturing torsional resonances with Timoshenko beams. In the nonlinear unsteady analysis, we found excellent agreement in capturing the damped natural frequency, but differences in the methods of structural damping between the the Timoshenko beam formulation and geometrically exact beam theory prevented a an exact comparison of the damped amplitudes.

When modeling the Sandia 34m VAWT, we found agreement in the resonance predictions, including rotational effects, through a Campbell diagram analysis with a maximum error of 8% for parked modes and 17% at the highest RPM for the highest blade mode, which may be attributed to the lack of aerodynamic damping in the modal analysis. Static loading from gravitational and centrifugal effects were compared with a high level of accuracy, and we discussed the sensitivity of minor blade shape variations on the centrifugal stress for this type of turbine. We recreated an approximation of the turbulent inflow velocity, drivetrain, and generator and showed agreement with the attenuated torque, flapwise, and lead-lag bending data from legacy experiments for a range of operating conditions and locations along the blades with errors ranging from less than 1% to 15%.

In summary, we found a strong ability for OWENS to predict mean and varying loads for a large land-based VAWT despite uncertainties in the turbulent inflow and drivetrain models. Based on the performance of the OWENS code with the presented validation cases, there is high level of trust in two-way coupled aeroelastic predictions using the OWENS software to enable simulation with adequate accuracy for design and certification of vertical-axis wind turbines.

Code Availability: The OWENS code is freely available at https://github.com/sandialabs/OWENS.jl, and many of the validation cases here have been incorporated into the code test suite.

Author Contributions: KRM performed the analyses, produced all figures, and drafted this report. BLE directed the work, advised and assisted in the model development and troubleshooting, and contributed significant edits to the report. All authors jointly finalized the report.

Acknowledgments: This work has been funded by the United States Department of Energy (DOE) Advanced Research Projects Agency – Energy (ARPA-e) under the ATLANTIS program.

This page intentionally left blank.

REFERENCES

[1] G. J. M. Darrieus. Turbine having its rotating shaft transverse to the flow of the current. U.S. Patent, Oct 1926. US1835018A.

[2] B F Blackwell, R E Sheldahl, and L V Feltz. Wind tunnel performance data for the darrieus wind turbine with naca 0012 blades. 5 1976.

[3] Robert E. Sheldahl, Paul C. Klimas, and Louis V. Feltz. Aerodynamic performance of a 5-metre-diameter darrieus turbine with extruded aluminum naca-0015 blades. Technical Report SAND-80-0179, Sandia National Laboratories, 3 1980.

[4] Mark H. Worstell. Aerodynamic performance of the doe/sandia 17-m-diameter vertical-axis wind turbine. *Journal of Energy*, 5(1):39–42, 1981.

[5] T D Ashwill. Measured data for the sandia 34-meter vertical axis wind turbine. 7 1992. SAND-91-2228.

[6] Alcoa. Design and fabrication of a low-cost darrieus vertical-axis wind-turbine system, phase ii. volume 2. final technical report. Technical report, 3 1983.

[7] PF Packman. Aging aircraft and fatigue failure. *J. Air L. & Com.*, 54:965, 1988.

[8] Delphine De Tavernier, Carlos Ferreira, and Anders Goude. *Vertical-Axis Wind Turbine Aerodynamics*, pages 1–45. Springer International Publishing, Cham, 2020.

[9] Rick Damiani, Dean Davis, and Brent Summerville. Aeroelastic modeling for distributed wind turbines: March 11, 2021 - november 10, 2021. 9 2022.

[10] A. Bianchini, G. Bangga, I. Baring-Gould, A. Croce, J. I. Cruz, R. Damiani, G. Erfort, C. Simao Ferreira, D. Infield, C. N. Nayeri, G. Pechlivanoglou, M. Runacres, G. Schepers, B. Summerville, D. Wood, and A. Orrell. Current status and grand challenges for small wind turbine technology. *Wind Energy Science*, 7(5):2003–2037, 2022.

[11] Maurizio Collu, Michael Borg, N.F. Rizzo, and Emilio Lupi. Flovawt: Further progresses on the development of a coupled model of dynamics for floating offshore vawts. volume 9, 06 2014.

[12] Zhengshun Cheng, Helge Aagaard Madsen, Zhen Gao, and Torgeir Moan. A fully coupled method for numerical modeling and dynamic analysis of floating vertical axis wind turbines. *Renewable Energy*, 107:604–619, 2017.

[13] Kai Wang, Torgeir Moan, and M. Hansen. A method for modeling of floating vertical axis wind turbine. volume 8, 06 2013.

[14] David Marten, Jan Wendler, Georgios Pechlivanoglou, Christian Navid Nayeri, and Christian Oliver Paschereit. Qblade: an open source tool for design and simulation of horizontal and vertical axis wind turbines. *International Journal of Emerging Technology and Advanced Engineering*, 3(3):264–269, 2013.

[15] David Marten, Matthew Lennie, Georgios Pechlivanoglou, Christian Paschereit, Norbert Dy, Ion Paraschivoiu, and Farooq Saeed. Validation and comparison of a newly developed aeroelastic design code for vawt. 01 2017.

[16] L. Meirovitch. *Computational Methods in Structural Dynamics*. Stijhoff and Noordhoff International Publishers, Rockville, Maryland, 1980.

[17] Brian C. Owens. *Theoretical Developments and Practical Aspects of Dynamic Systems in Wind Energy Applications*. PhD thesis, Texas A&M, 2013.

[18] Jeff Bezanson, Alan Edelman, Stefan Karpinski, and Viral B Shah. Julia: A fresh approach to numerical computing. *SIAM review*, 59(1):65–98, 2017.

[19] Kevin R. Moore and Brandon L. Ennis. Vertical-axis wind turbine steady and unsteady aerodynamics for curved deforming blades. *AIAA Journal*, 60(1):189–196, 2022.

[20] Jonathan Murray and Matthew Barone. *The Development of CACTUS, a Wind and Marine Turbine Performance Simulation Code*.

[21] NREL. Openfast. open-source wind turbine simulation tool, available at http://github.com/openfast/openfast, 2022.

[22] G. S. Bir. *User's guide to OWENSPreComp (Pre-Processor for Computing Composite Blade Properties)*. National Renewable Energy Laboratory, 2006.

[23] W.L. Oberkamph, T.G. Trucano, and C. Hirsch. Verification, validation, and predictive capability in computational engineering and physics. Technical Report SAND2003-3769, Sandia National Laboratories, 2003.

[24] Wenbin Yu and Maxwell Blair. Gebt: A general-purpose nonlinear analysis tool for composite beams. *Composite Structures*, 94(9):2677–2689, 2012. https://github.com/byuflowlab/GXBeam.jl.

[25] Daniel J. Inman. *Engineering Vibrations*, chapter 6, pages 539, 608. Pearson, 4th edition, 2014. ISBN-13:9780132871723.

[26] Taylor McDonnell and Andrew Ning. Gxbeam: A pure julia implementation of geometrically exact beam theory. *Journal of Open Source Software*, 7(73):3997, May 2022.

[27] Qi Wang, Wenbin Yu, and Michael Sprague. *Geometric Nonlinear Analysis of Composite Beams using Wiener-Milenković Parameters*. AIAA, 2013.

[28] Dewey H. Hodges. Nonlinear composite beam theory. 2006.

[29] Barry J. Goodno James M. Gere. *Mechanics of Materials*, chapter 9, page 805. Cengage Learning, 2013. ISBN-13: 978-81-315-2474-9.

[30] Herbert J. Sutherland. Strain gauge validation experiments for the sandia 34-meter vawt test bed. Technical Report SAND-88-1807, Sandia National Laboratories, 1988.

[31] N D Kelley and B J Jonkman. Overview of the turbsim stochastic inflow turbulence simulator: Version 1.10. 9 2006.

[32] Christopher Lee Kelley and Brandon Lee Ennis. Swift site atmospheric characterization. 1 2016.

DISTRIBUTION

Email—Internal

Name	Org.	Sandia Email Address
Technical Library	1911	sanddocs@sandia.gov

Sandia National Laboratories is a multimission laboratory managed and operated by National Technology & Engineering Solutions of Sandia LLC, a wholly owned subsidiary of Honeywell International Inc., for the U.S. Department of Energy's National Nuclear Security Administration under contract DE-NA0003525.